The structure and thermoelectric properties of tungsten bronze $Ba_6Ti_2Nb_8O_{30}$

Dongting Jiang (iD), Dursun Ekren, Feridoon Azough, Sarah J. Day, Kan Chen, Amit Mahajan, Demie M. Kepaptsoglou (iD), Quentin M. Ramasse (iD), Michael J. Reece, and Robert Freer (iD)

COLLECTIONS

Paper published as part of the special topic on Advanced Thermoelectrics
Note: This paper is part of the special topic on Advanced Thermoelectrics.

View Online   Export Citation   CrossMark

ARTICLES YOU MAY BE INTERESTED IN

Space-charge-induced Seebeck effect in solid dielectrics
Journal of Applied Physics **126**, 125106 (2019); https://doi.org/10.1063/1.5117190

Large enhancement of thermoelectric performance of InTe compound by sintering and $CuInTe_2$ doping
Journal of Applied Physics **126**, 125108 (2019); https://doi.org/10.1063/1.5117500

Study of TaN and TaN-Ta-TaN thin films as diffusion barriers in $CeFe_4Sb_{12}$ skutterudite
Journal of Applied Physics **126**, 125306 (2019); https://doi.org/10.1063/1.5105385

Lock-in Amplifiers
... and more, from DC to 600 MHz
Watch

The structure and thermoelectric properties of tungsten bronze $Ba_6Ti_2Nb_8O_{30}$

Dongting Jiang,[1] (iD) Dursun Ekren,[1] Feridoon Azough,[1] Sarah J. Day,[2] Kan Chen,[3] Amit Mahajan,[3]
Demie M. Kepaptsoglou,[4,5] (iD) Quentin M. Ramasse,[4,6] (iD) Michael J. Reece,[3] and Robert Freer[1,a] (iD)

AFFILIATIONS

[1]School of Materials, University of Manchester, Manchester M13 9PL, United Kingdom
[2]Diamond Light Source, Harwell Science and Innovation Campus, Oxfordshire OX11 0DE, United Kingdom
[3]School of Engineering and Materials Science, Queen Mary University of London, London E1 4NS, United Kingdom
[4]SuperSTEM Laboratory, STFC Daresbury Campus, Daresbury WA4 4AD, United Kingdom
[5]Jeol Nanocentre and Department of Physics, University of York, Heslington, York YO10 5DD, United Kingdom
[6]School of Chemical and Process Engineering and School of Physics, University of Leeds, Leeds LS2 9JT, United Kingdom

Note: This paper is part of the special topic on Advanced Thermoelectrics.
[a]**Author to whom correspondence should be addressed**: Robert.Freer@manchester.ac.uk

ABSTRACT

Tungsten bronze (TB) structured materials have attracted attention as possible thermoelectrics because of their complex crystal structure. In this work, a new thermoelectric ceramic with a tetragonal tungsten bronze (TB) structure, $Ba_6Ti_2Nb_8O_{30}$ (BTN), was prepared by the conventional mixed oxide route with some samples processed by Spark Plasma Sintering (SPS). The addition of MnO enabled the fabrication of high density BTN ceramics at a low sintering temperature of 1580 K in air and by SPS. All samples were annealed in a reducing atmosphere after sintering. X-ray diffraction showed that $Ba_6Ti_2Nb_8O_{30}$ crystallizes with tetragonal symmetry (*P4bm* space group). High angle annular dark field-electron energy loss spectroscopy analysis confirmed the proposed crystal structure and provided exact elemental distributions in the lattice, showing higher concentrations of Ti in the 2b lattice sites compared to the 8d lattice sites. XPS showed the presence of two spin-orbit double peaks at 207.7 eV in the reduced BTN samples, confirming the presence of Nb^{4+} ions. By the use of a sintering aid and optimization of the processing parameters, the ceramics achieved a high power factor of $280\,\mu W/m\,K^2$ at 873 K. The BTN ceramics showed phonon-glass-type thermal conduction behavior with a low thermal conductivity of 1.7–1.65 W/m K at 300–873 K. A thermoelectric figure of merit (ZT) of 0.14 was achieved at 873 K. This ZT value is comparable with results for many TB thermoelectrics. However, BTN has the advantage of much easier processing.

I. INTRODUCTION

Thermoelectric (TE) materials can transform thermal energy to electrical energy and can, therefore, be exploited in a range of applications from energy harvesting to cooling devices. Candidate materials are usually screened by their thermoelectric figure of merit, ZT, which is based on the Seebeck coefficient S, the electrical conductivity σ, and the thermal conductivity κ, and embodied in the equation $ZT = \sigma S^2 T/\kappa$, where T is the absolute temperature.[1] Current commercial devices usually employ Bi- and Pb-based telluride thermoelectric materials, which exhibit high ZT values, ~1 at

room temperature.[2–4] However, these materials have disadvantages; narrow temperature range for maximum performance, poor structural stability at high temperature, and containing toxic and/or rare elements. In the last two decades, oxides have attracted increasing attention for thermoelectric applications due to their chemical stability, low cost, and ease of preparation. Among the oxides, a number of tungsten bronze (TB) structured materials in the (Sr,Ba)Nb_2O_6 system, mainly based on $Sr_{0.61}Ba_{0.39}Nb_2O_6$ (SBN61), have been investigated as possible thermoelectrics because their complex crystal structure encourages low thermal conductivity. Lee *et al.*[5]

determined the thermoelectric properties of single crystal SBN61 and confirmed a high power factor, σS^2, along the c-direction (2×10^{-3} W/m K^2 at 516 K). However, the anisotropic properties of these materials suggested that texturing of ceramics would be necessary to maximize thermoelectric performance. They concluded that the conduction mechanism for highly reduced samples was polaron hopping. Lee et al.[6] also prepared textured polycrystalline SBN61 ceramics using a templated grain growth approach and showed that both σ and S were higher along the c-axis. The properties of nontextured ceramics were limited by the characteristics measured along the a-axis, with S values being independent of temperature.

By the introduction of fluorine at oxygen sites of SBN61, Li et al.[7] were able to significantly increase the carrier concentration and modify the band structure, leading to increased σ and the reduction in S. Fluorine doping had the additional benefit of reducing thermal conductivity. Ceramics of formulation $Sr_{0.61}Ba_{0.39}Nb_2O_{5.95}F_{0.05}$ exhibited the best thermoelectric performance due to the combination of high σS^2 and relatively low κ, leading to a maximum ZT of 0.21 at 1073 K.

Interstitial doping of SBN ceramics has also been explored as a way to improve thermoelectric performance.[8,9] Azough et al.[10] investigated a related ferroelectric ceramic with the TB structure $Ba_{6-x}Nd_{8+2x}Ti_{18}O_{54}$ and evaluated the effect of the Ba/Nd ratio on thermoelectric properties. They demonstrated that $Ba_{5.19}Nd_{8.54}Ti_{18}O_{54}$ exhibited a high S value ($-210\,\mu$V/K) and an acceptable σ (60 S/cm), which led to a maximum power factor of 2.5×10^{-4} W/m K^2 at 1000 K. Furthermore, this material exhibited a low and stable thermal conductivity over the full measurement range, being only 1.45 W/m K at 1000 K, one of the lowest values reported for thermoelectric oxides. A maximum ZT of 0.16 was obtained at 1000 K. These results for $Ba_{6-x}Nd_{8+2x}Ti_{18}O_{54}$ ceramics are promising; texturing and different doping strategies could further improve the properties.

The structure of $Ba_6Ti_2Nb_8O_{30}$ (BTN) ceramic was first reported in 1965.[11] BTN has a tetragonal structure with space group $P4bm$,[11] with lattice parameters $a = b = 12.53$ Å and $c = 4.01$ Å. The structure consists of NbO$_6$ octahedra sharing corners occupied by Nb and Ti forming two main interstices (A1 and A2).[11] In BTN, both pentagonal A1-sites and tetragonal A2-sites are predominantly occupied by Ba. The co-existence of pentagonal and tetragonal sites results in trigonal vacant c-sites in the structure (Fig. 1). BTN ceramic was initially studied as a ferroelectric due to its low dielectric loss and low temperature coefficient of relative permittivity.[12,13] Building on the earlier work of Azough et al.[10] on TB materials, we have investigated the crystal structure and, for the first time, the thermoelectric properties of ceramic $Ba_6Ti_2Nb_8O_{30}$. We employed MnO as a sintering aid to reduce the processing temperatures and increase the sample quality. Selected samples were fabricated by Spark Plasma Sintering (SPS) to achieve high density with the possibility of developing texture; the electrical conductivity and Seebeck coefficients are usually maximized along the c-axis for tetragonal tungsten bronze structured materials.[5] The exact crystal structure of $Ba_6Ti_2Nb_8O_{30}$ was unambiguously determined by combined high resolution X-ray diffraction and aberration-corrected atomic resolution analytical Scanning Transmission Electron Microscopy (STEM).
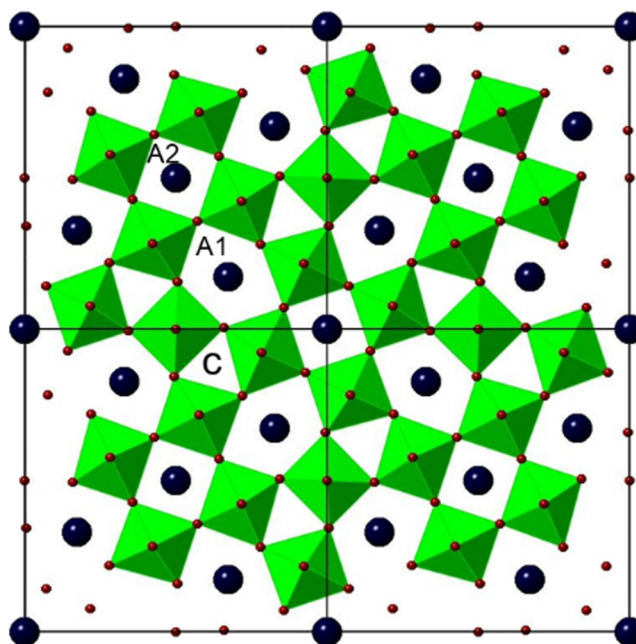

FIG. 1. A 2 × 2 unit cell [001] projection of the structure of BTN showing NbO$_6$ octahedra (green). Red circles in the corners of the octahedral are oxygen atoms, A1 and A2 interstitial sites occupied by Ba atoms (black circles) and vacant c-sites.

II. EXPERIMENTAL

$Ba_6Ti_2Nb_8O_{30}$ ceramics were prepared from high-purity powders of BaCO$_3$ (Sigma Aldrich, 99.9%), TiO$_2$ (Sigma Aldrich, 99.9%), and Nb$_2$O$_5$ (Acros Organics, 99.9%). The raw powders were mixed according to the target composition and wet milled for 24 h using zirconia balls and propan-2-ol. The mixture was dried at 358 K for 24 h and then calcined at 1273 K in air for 8 h. Manganese oxide (equivalent to 0.5 wt. %) in the form of MnCO$_3$ (Sigma Aldrich, 99.9%) was added to the calcined powder as a sintering aid. The powders were then remilled and dried using the same conditions described above. For conventional sintering, the calcined powders were uniaxially pressed into pellets of 20 mm diameter and 5 mm thickness and sintered in air at 1573 K for 4 h. Some samples were subsequently annealed in an Ar (5-mol. % H$_2$) atmosphere at 1573 K for 6 or 12 h. The samples are denoted as BTN-S, BTN-A6, and BTN-A12, respectively ("S" denotes sintered, "A" indicates annealed samples, and the final number the duration in hours). Selected samples were processed by SPS using a HPD 25/1, FCT systems (Germany) SPS furnace at Queen Mary, University of London. The same stock calcined powders were placed into a graphite die of 20 mm diameter (obtained from Erodex®) and sintered for 5 min at 1523 K with a pressure of 16 MPa and a cooling rate of 323 K/min. Such samples are denoted as BTN-SPS-S. The as-sintered SPS samples were also annealed in an Ar (5-mol. % H$_2$) atmosphere at 1473 K for 12 or 24 h; the samples are denoted as BTN-SPS-A12 and BTN-SPS-A24,

respectively. The SPS samples were annealed at a lower temperature than conventionally processed samples to minimize problems caused by the second phase development.

Cu radiation, X-ray diffraction (XRD) analysis was carried out using a PANanalytical X'Pert Pro diffractometer. High resolution synchrotron X-ray diffraction analysis was carried out at the Diamond Light Source (beamline I11) with radiation of the wavelength of 0.826 013(10) Å; calibration employed a NIST SRM640c standard reference material. Crystal structure refinement was carried out using TOPAS 4.2 software (Bruker AXS, Karlsruhe, Germany).[14] Scanning electron microscopy (SEM) of polished sample surfaces was undertaken using a Philips XL30 FEGSEM equipped with an energy dispersive X-ray (EDX) detector. An FEI FEGTEM (Tecnai G30) transmission electron microscopy (TEM) was initially used to analyze the microstructure and crystal structure of materials. Subsequently, atomic resolution structural characterization was carried out using an aberration-corrected Nion microscope (UltraSTEM100; Nion Company, Kirkland, WA), located at the Daresbury SuperSTEM Laboratory in the UK.

Electrical transport properties, Seebeck coefficients and electrical conductivity, were determined from 350 to 873 K in a helium atmosphere using a ULVAC-RIKO ZEM-3 facility. For thermal property measurements, thermal diffusivity (α) was measured by the laser flash technique using a Netzsch LFA427 Laser Flash Analyser. Heat capacity (C_p) was measured in an argon atmosphere using a Netzsch STA 449C. Sample densities (ρ) were determined by the Archimedes method. The thermal conductivity (k) was calculated from the product of thermal diffusivity, heat capacity, and density using $\kappa = \alpha \, C_p \, \rho$.

III. RESULTS AND DISCUSSION

A. Conventional pressureless sintering

1. Microstructure and crystal structure

The air-sintered $Ba_6Ti_2Nb_8O_{30}$ ceramic samples are light brown in color. Upon annealing in a reducing atmosphere, the color changes to dark gray, indicating the reduction of Nb^{5+} and Ti^{4+} to lower valance states.[15] All three types of samples (BNT-S, BNT-A6, and BNT-A12) achieved densities of at least $95.5 \pm 0.3\%$ theoretical.

To evaluate the sample microstructures after sintering and annealing, SEM characterization was initially performed. Figure 2(a) shows a secondary electron image of air-sintered BTN-S; the samples are single phase and exhibit equiaxed grains with an average grain size of $8.4\,\mu$m. Upon annealing, the grain morphology for BTN-S was unchanged [Fig. 2(b)], but the grain sizes of BTN-A6 and BTN-A12 were significantly larger at 14.9 and $15.2\,\mu$m, respectively [Figs. 2(c) and 2(d)]. However, the formation of a minor secondary phase, plate shaped and darker in contrast compared to that of the matrix phase, occurred in the latter two samples [indicated by arrows in Figs. 2(c) and 2(d)]. EDX analysis confirmed the presence of Ba, Ti, and Nb in the secondary phase with the atomic ratios of approximately 2:1:1, equivalent to $Ba(Ti_{0.46}Nb_{0.54})O_3$; this phase is richer in Ti than the primary phase (see also Fig. S-1 in the supplementary material).

In order to clarify and resolve details of the structural data obtained by XRD for the BTN air-sintered sample[11,16–18] and understand the structural changes arising after annealing, high
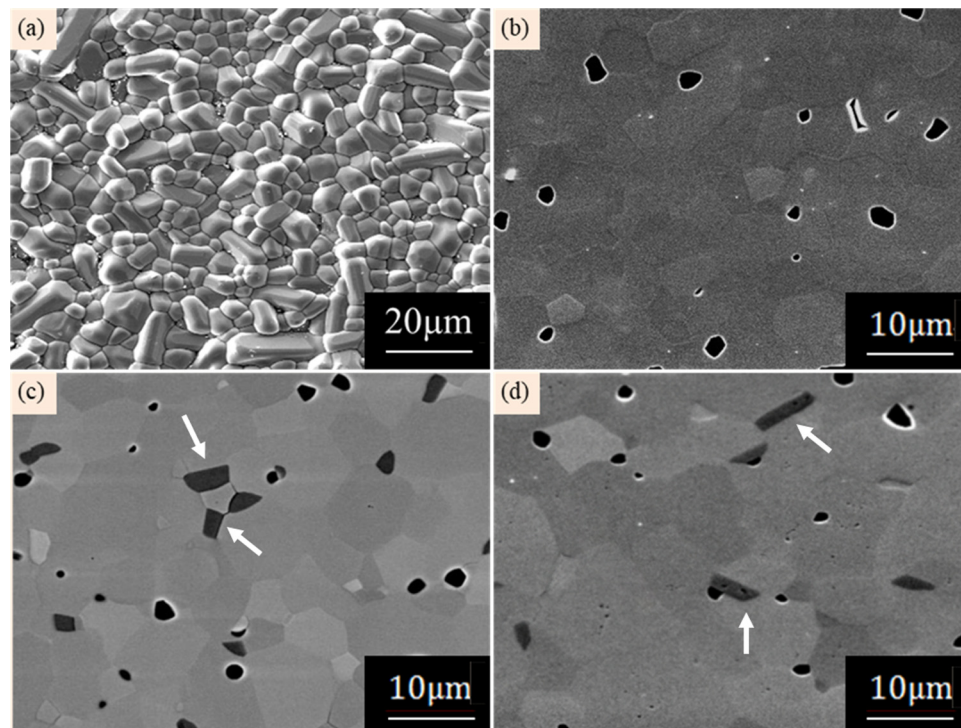

FIG. 2. (a) Secondary electron (SE) image for the as-fired surface of air-sintered BTN-S. Backscattered electron (BSE) images of sintered and annealed (polished) samples of (b) BTN-S, (c) BTN-A6, and (d) BTN-A12.

precision STEM imaging and analysis and atomically resolved chemical mapping were performed for BTN-S and BTN-A12 samples. [001] zone axis high angle annular dark field (HAADF) images and the electron energy loss spectroscopy (EELS) maps for the BTN-S sample are presented in Figs. 3(a)–3(d). The HAADF image in Fig. 3(a) shows a uniform distribution of the four types of "compositional" columns with different intensities inside the red circles [top left region of Fig. 3(a)]. EELS mapping reveals that the bright columns in the HAADF image represent Ba ($Z = 56$) shown inside circles in Fig. 3(a), and the columns with lower intensity represent Ti ($Z = 22$) or Nb ($Z = 41$). The areas with darkest intensity and triangular shape are believed to be normally vacant c-sites of
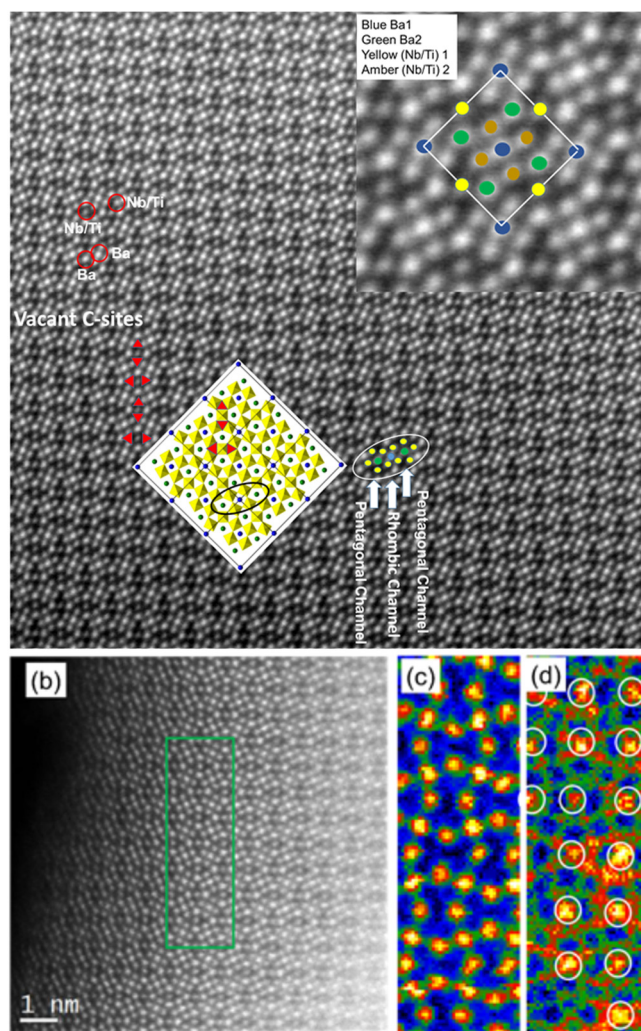
the TB structure. The Ba columns are coordinated with 5 or 4 Ti/Nb columns, presenting pentagonal and tetragonal channels of the structure, as shown inside ellipsoid in the bottom of Fig. 3(a). The HAADF image comprises the repeating segments of Ba columns coordinated with 5 Ti/Nb columns (pentagonal channels) and 4 Ti/Nb (tetragonal channels). Two pentagonal channels are at the end of the segment, with one tetragonal channel in between. The HAADF images agree with the structural model of $Ba_6Ti_2Nb_8O_{30}$ (ICSD card No. 151418) and are included in the lower central region of Fig. 3(a). The unit cell is superimposed on the HAADF image in the top right inset of Fig. 3(a). A very good match for the site occupancies of the constituent elements between the HADDF image and the proposed crystal structure can be seen (ICSD card No. 151418).

The Ba and Ti EELS maps [Figs. 3(c) and 3(d)], obtained from the region highlighted in Fig. 3(b), show that the A sites (pentagonal and tetragonal channels) are occupied by Ba and the B sites are occupied by Ti. There is a homogeneous distribution of Ba in both channels, while the distribution of Ti is nonuniform; Ti has a higher concentration in (Ti/Nb)2 sites compared to the (Ti/Nb)1 sites.

To investigate the structural changes and the stability of $Ba_6Ti_2Nb_8O_{30}$ after annealing in the reducing atmosphere, [001] zone axis HAADF images and EELS maps for the BTN-A12 sample were collected. The HAADF image for the BTN-A12 sample [shown in Fig. 4(a)] is similar to the HAADF image for BTN-S [Fig. 3(a)], suggesting that the structural arrangement of $Ba_6Ti_2Nb_8O_{30}$ has not changed upon annealing. The Ba and Ti EELS maps [Figs. 4(c) and 4(d)] suggest that, similar to BTN-S, the A sites are occupied by Ba and the B sites are occupied by Ti/Nb. Again the Ba data show a homogenous distribution, while the distribution of Ti is nonuniform; the Ti concentrations in Ti/Nb 2 sites are higher.

A significant observation from HAADF imaging is the presence of the structural linear defect in the Ar annealed ceramics; Fig. 5 presents data for BTN-12 as an example. The corresponding HAADF-EELS data for the linear defect (shown in Fig. 6) reveal that the linear defect is deficient in Ba, and the related tetragonal channel is distorted. Thus, annealing promoted lattice distortion of the tungsten bronze structure of BTN-A12.

Following initial X-ray diffraction analysis using Cu radiation, high resolution synchrotron X-ray diffraction analysis was carried out. Figure 7 shows the Rietveld refinement of the spectra collected for BTN-S and BTN-A12. Data for both samples were refined for tetragonal symmetry with *P4bm* as the space group. The refinement details and lattice parameters are summarized in Table I. The lattice parameters for the base material, BTN-S, agree with the data of Jamieson and Abrahams[18] and Stephenson.[11] The data for sample BTN-A12 show that the annealing process led to structural changes, causing the *a* lattice parameter to increase by 0.024 Å and the *c* lattice parameter to decrease by 0.017 Å. For BTN-S, the value of $\sqrt{10}\, c/a = 1.01$, i.e., >1. As this value differs from 1, it indicates that the BO_6 octahedra are distorted; the *c* value reflects the height of the octahedra.[17] The distortion is caused by the displacement of cations in BO_6 octahedra resulting in a net effective distortion along the [001] direction.[17] For BTN-A12, the value of $\sqrt{10}\, c/a$ is smaller, but is still greater than 1. This indicates that the BTN ceramics still show octahedral distortion after reduction.

FIG. 3. [001] HAADF image and EELS data for BTN-S ceramic. (a) Top right inset is the superimposition of the proposed crystal structure obtained by XRD on the HAADF image. (b) HAADF image with the green rectangle showing the area used for chemical analysis. (c) and (d) EELS maps for Ba and Ti, respectively.
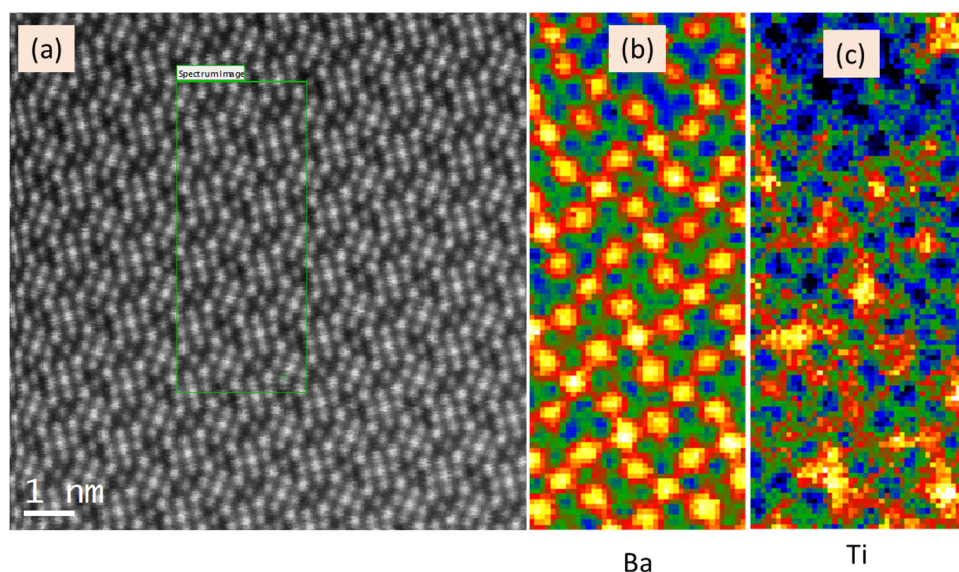
FIG. 4. [001] HAADF and EELS data for BTN-S ceramic. (a) HAADF image showing the area in a green rectangle used for chemical analysis. EELS maps for (b) Ba and (c) Ti map.

Full details of the refined atomic positions and thermal parameters for BTN-S and BTN-A12 are presented in Table S-1 in the supplementary material. The positional parameters for BTN-S are in good agreement with the data of Jamieson and Abrahams[18] and Stephenson.[11] Upon annealing $Ba_6Ti_2Nb_8O_{30}$, the B1 site atoms show a significant positional movement (11%) along the z direction. This is believed to be responsible for the change in lattice parameter c, which is equivalent to the height of the octahedra. For BTN-S, the total occupancy of B sites by Ti and Nb atoms was 1.98 and 8.02, respectively, which is consistent with the stoichiometry of $Ba_6Ti_2Nb_8O_{30}$. However, for BTN-A12, the Ti occupancy was significantly lower, approximately 18.6%. This change is related to the formation of the Ti-rich secondary phase, $Ba(Ti_{0.46}Nb_{0.54})O_3$, which represents 4.41(3)% of the sample; this fraction of secondary phase will reduce the Ti occupancy of the main phase by around 1%. Annealing causes changes in the oxygen site occupancy in the Ba-Ti-Nb-O system. There was a decrease of 3%–4% in occupancies of the O(1), O(4), and O(5) positions, while O(2) and O(3) occupancies were unchanged. This indicates that the oxygen atoms in the former positions are more likely to be lost during annealing in the reducing atmosphere. This is consistent with the preferential location for oxygen vacancy formation in the Sr-Ba-Nb-O system (O 4c site).[19]
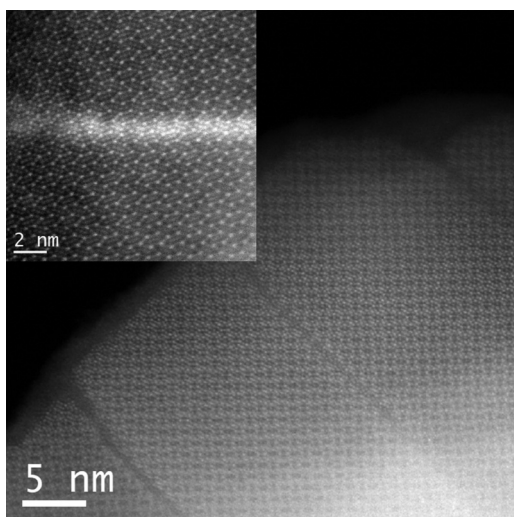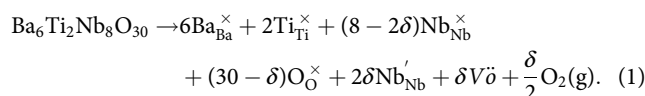
2. XPS analysis

XPS was used to determine the oxidation state of Nb in the $Ba_6Ti_2Nb_8O_{30}$ samples before and after reduction. Figure 8 shows the XPS peaks of Nb $3d_{5/2}$ and $3d_{3/2}$ for BTN-S and BTN-A12. Peaks corresponding to Nb $3d_{5/2}$ and $3d_{3/2}$ are located at 206.8 eV and 209.5 eV, respectively. The spin-orbital peak separation was 2.7 eV in agreement with the work of Nefedov et al.[20] BTN-A12 shows extra shoulders in the XPS spectrum at a lower binding energy of 207.7 eV, which corresponds to the Nb^{4+} oxidation state,[20] which was not present in the spectrum of BTN-S. This confirms that the Nb^{5+} ions in BTN-S were reduced to Nb^{4+} during the annealing processing. Additionally, the presence of only Ti^{4+} was evident from the Ti 3d spectrum (see Fig. S-2 in the supplementary material). Thus, the charge compensation due to reduction annealing can be represented by Eq. (1) in terms of the Kroger-Vink notation,

FIG. 5. [001] HAADF image showing the linear defect in the BTN-A12 sample. The MAADF image of the boundary area is shown as the inset.

$$Ba_6Ti_2Nb_8O_{30} \rightarrow 6Ba_{Ba}^{\times} + 2Ti_{Ti}^{\times} + (8 - 2\delta)Nb_{Nb}^{\times}$$
$$+ (30 - \delta)O_O^{\times} + 2\delta Nb_{Nb}' + \delta V\ddot{o} + \frac{\delta}{2}O_2(g). \quad (1)$$
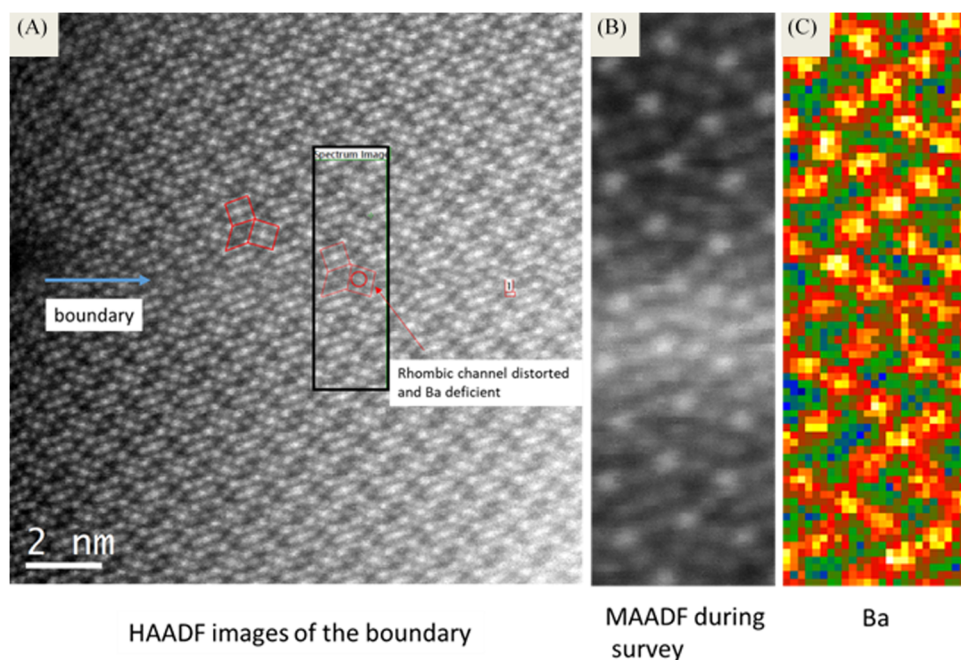
FIG. 6. [001] HAADF-EELS data for the linear defect in sample BTN-A12 (see Fig. 5). (a) HAADF image, (b) MADDF image during data collection, and (c) Ba EELS map.

Extra charge carriers will be generated by the reduction process, and hence an enhancement in the electrical conductivity is expected. For BTN-A12, the amount of Nb^{4+} present was calculated to be around 1.1%, while for air-sintered BTN, the Nb^{4+} concentration was too small to detect. On this basis, the oxygen deficiency for BTN-A12 was calculated; the BNT formula can be rewritten as $Ba_6Ti_2Nb_8O_{29.9945}$, where the average Nb valance is 4.989.
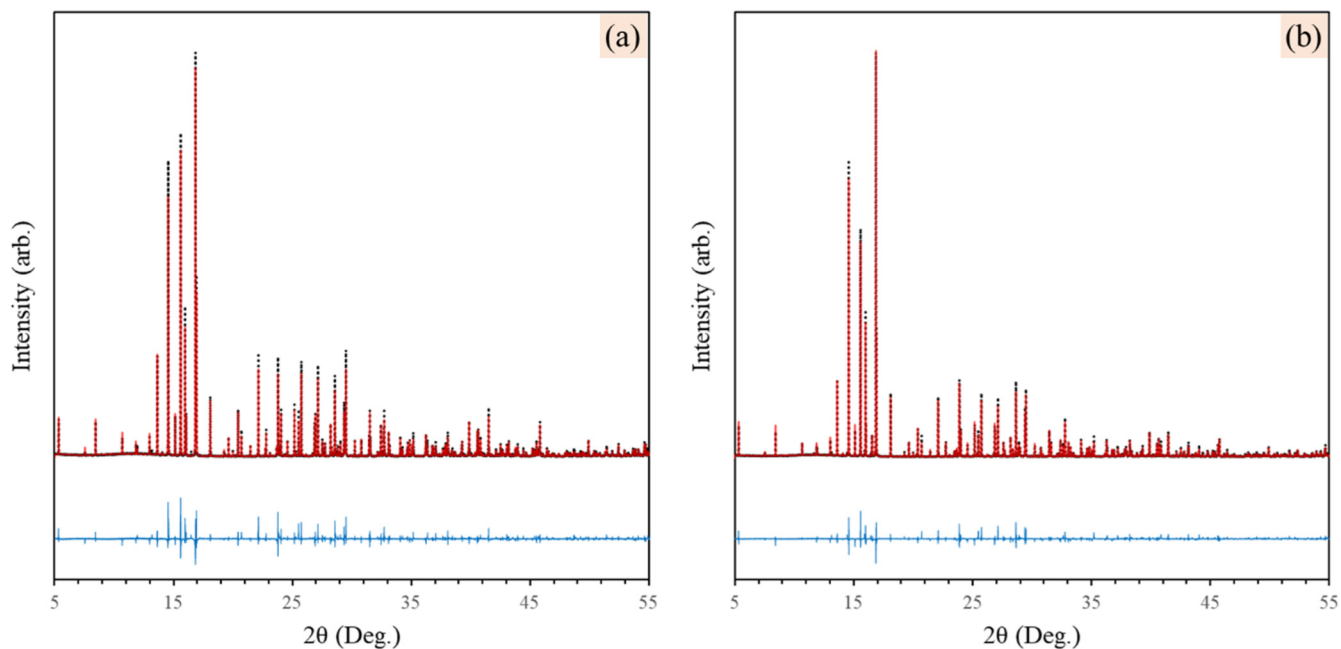

FIG. 7. Refined synchrotron diffraction data for (a) BTN-S and (b) BTN-A12. Experimental data are presented by the blue dashed line, the refined profile by the red line, and the difference by the (lower) blue line.

TABLE I. Refinement parameters and lattice parameters for BTN-S and BTN-A12.

Sample	BTN-S	BTN-A12
R-values and GOF	$R_{exp} = 7.8$, $R_{wp} = 14.43$, GOF $= 1.85$	$R_{exp} = 7.29$, $R_{wp} = 12.81$, GOF $= 1.76$
Lattice parameters (Å)	$a = 12.540\ 736(9)$, $c = 4.007\ 021(6)$	$a = 12.564\ 320(10)$, $c = 3.990\ 353(5)$

3. Thermoelectric properties

The temperature dependency of thermoelectric properties of reduced $Ba_6Ti_2Nb_8O_{30}$ ceramics (BTN-A6 and BTN-A12) is shown in Fig. 9. It is clear that the electrical conductivity of $Ba_6Ti_2Nb_8O_{30}$ is dependent on the annealing time [Fig. 9(a)], increasing from 44 S/cm at 350 K to 91 S/cm at 873 K with increasing the annealing time from 6 h to 12 h. Longer annealing time under reducing
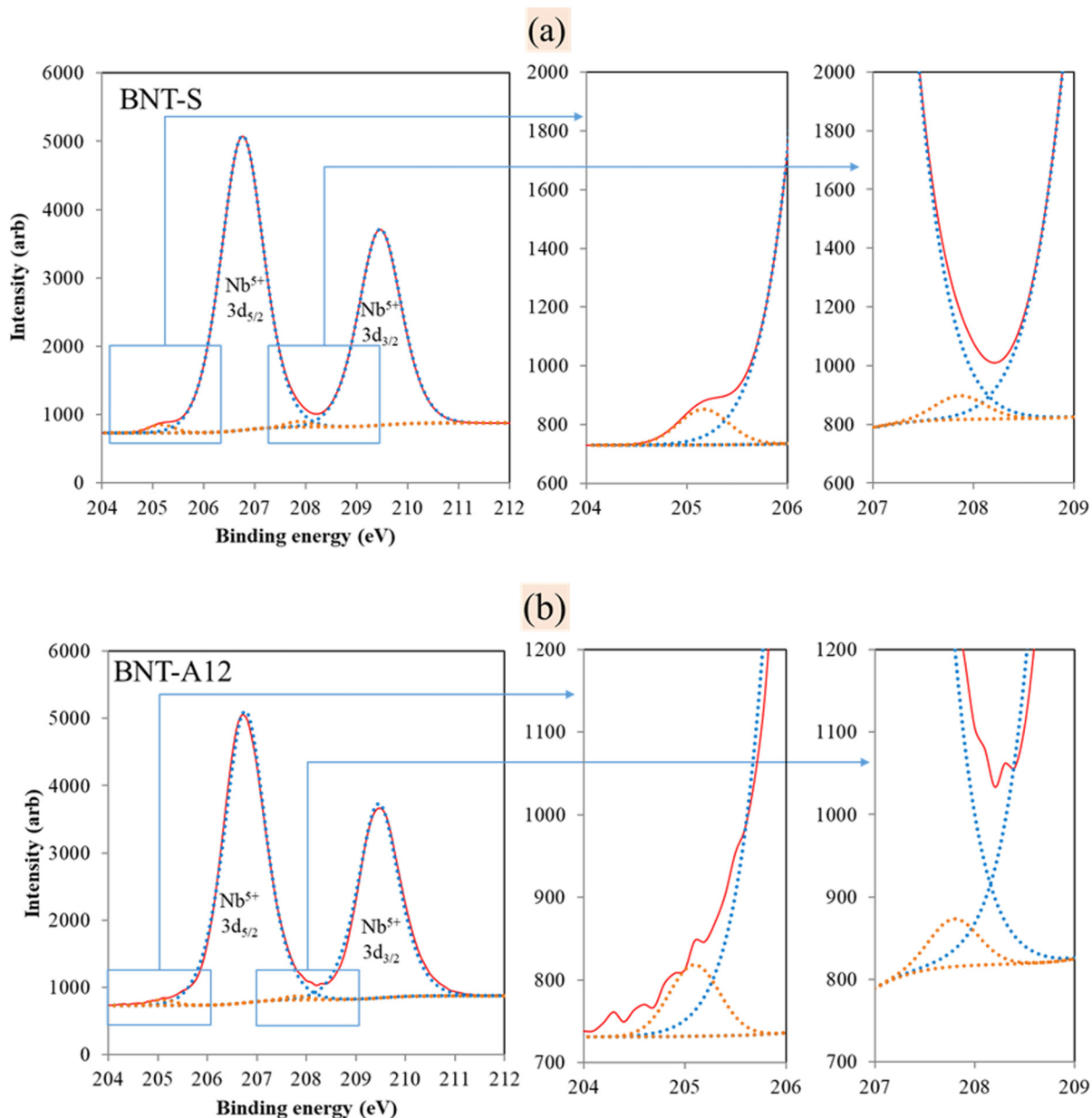

FIG. 8. (a) XPS spectra for air-sintered $Ba_6Ti_2Nb_8O_{30}$ showing only the presence of Nb^{5+} and (b) XPS spectra for BTN-A12 showing the presence of both Nb^{5+} and Nb^{4+}.
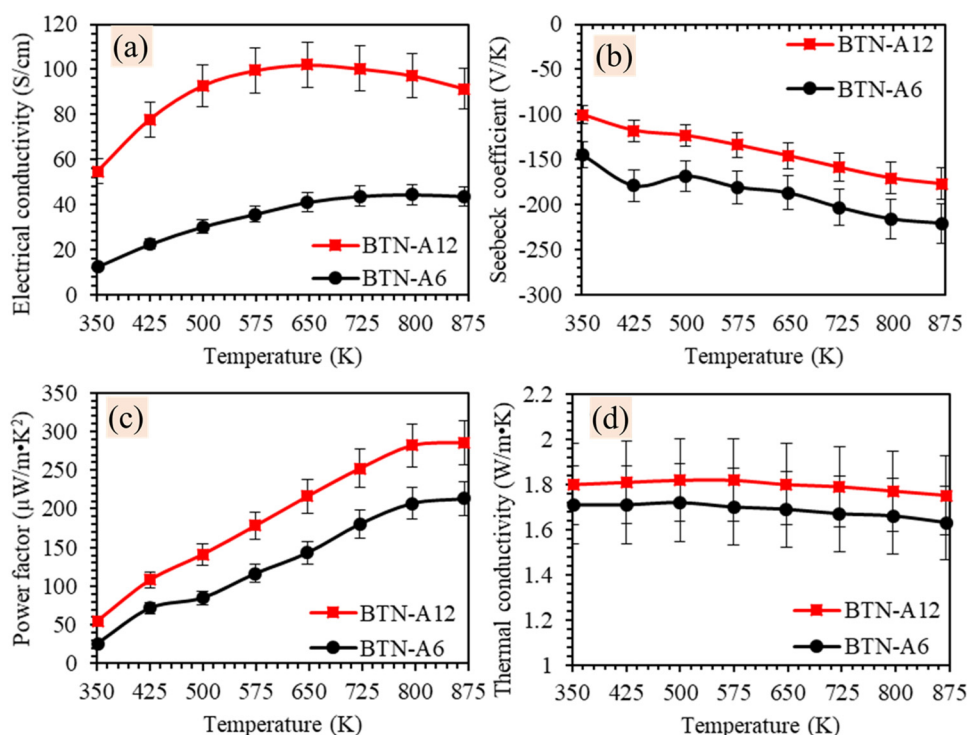
FIG. 9. The temperature dependence of (a) electrical conductivity, (b) Seebeck coefficient, (c) power factor, and (d) thermal conductivity for BTN-A6 and BTN-A12 samples prepared by the mixed oxide route.

conditions led to a higher concentration of oxygen vacancies (Fig. 8) and increased carrier concentration [Eq. (1)]. In addition, the reduction in the c lattice parameter is expected to encourage the orbital overlap, which could potentially enhance the carrier mobility along the c-axis; this is usually the direction along which the highest σ is observed for TB structured materials.[5,21] Both BTN-A6 and BTN-A12 samples exhibited negative Seebeck coefficients [Fig. 9(b)], confirming the n-type nature of BTN. The Seebeck coefficients increase steadily with temperature. $|S|$ values for BTN-A12 are lower because of the higher carrier concentration and electrical conductivity. Consequently, the power factor (σS^2) values for both samples increase with increasing temperature [Fig. 9(c)]. BTN-A12 shows a higher power factor ($\sim 286\,\mu\text{W/m K}^2$) than BTN-A6 at 873 K.

Both BTN-A6 and BTN-A12 exhibit a low and temperature stable total thermal conductivity of about 1.5–1.75 W/m K at 873 K [Fig. 9(d)]. The electronic component of thermal conductivity κ_e can be obtained from the Wiedemann-Franz relationship given by Eq. (2),

$$\kappa_e = \sigma L_o T, \qquad (2)$$

where L_o is the Lorenz number (equal to $2.45 \times 10^{-8}\,\text{W}\,\Omega/\text{K}^2$), σ is the electrical conductivity, and T is the absolute temperature. The calculated values of κ_e for BTN-A6 and BTN-A12 are very small, around $0.6-1.7 \times 10^{-3}$ W/m K, which translates to a contribution of less than 0.1% to total κ. Therefore, it can be concluded that the low thermal conductivity for BTN-A6 and BTN-A12 can be attributed to

their low lattice thermal conductivity. $\text{Ba}_6\text{Ti}_2\text{Nb}_8\text{O}_{30}$ has a complex crystal structure and the presence of heavy of cations (Ba^{2+} and Nb^{5+}) in different sublattices will promote phonon scattering. Additionally, the existence of vacant c-sites (Fig. 3) will enhance the scattering of phonons and help to reduce thermal conductivity.[22,23]

B. SPS sintering

1. Crystal structure and microstructure

The SPS-prepared $\text{Ba}_6\text{Ti}_2\text{Nb}_8\text{O}_{30}$ ceramics were all of high density $\sim 99\%$ theoretical. The dark gray color reflects preparation in the reducing atmosphere of SPS. Laboratory XRD (see Fig. S-3, supplementary material) confirmed that BTN-SPS-S has a tetragonal tungsten bronze structure with the $P4bm$ space group, and lattice parameters $a = b = 12.544(2)$ Å and $c = 3.989(4)$ Å. The structures of SPS-prepared BTN ceramics were unchanged after annealing, with limited variation in lattice parameters: $a = b = 12.549(2)$ Å and $c = 3.988(3)$ Å for BTN-SPS-A12, and $a = b = 12.549(4)$ Å and $c = 3.988(1)$ Å for BTN-SPS-A24. A secondary phase of BaTiO_3 with cubic symmetry and $Pm\bar{3}m$ space group was detected in all the three BTN-SPS samples. Another secondary phase of $\text{Ba}_2\text{Ti}_3\text{Nb}_4\text{O}_{18}$ with a monoclinic structure was also observed in BTN-SPS-A12 and BTN-SPS-A24.

BSE-SEM images of the SPS-prepared BTN ceramics are shown in Fig. 10. In the microstructure of all three SPS samples (BTN-SPS-S, BTN-SPS-A12, and BTN-SPS-A24), a minor secondary phase was observed, being brighter in contrast to the matrix. In addition, another minor phase, having a darker contrast, was
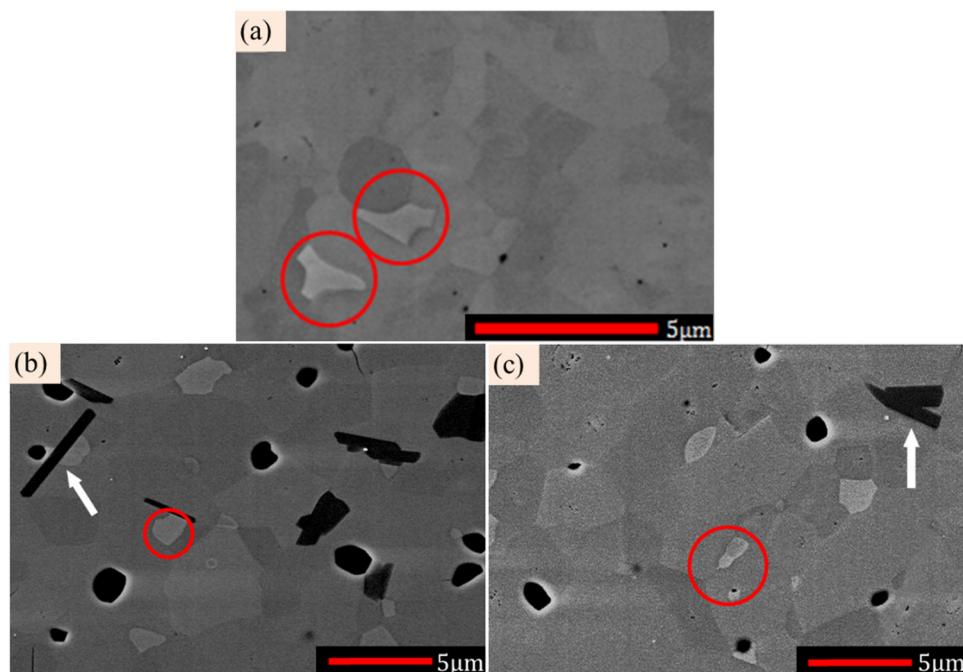
FIG. 10. BSE images of polished surfaces of $Ba_6Ti_2Nb_8O_{30}$ ceramics prepared by SPS: (a) BTN-SPS-S, (b) BTN-SPS-A12, and (c) BTN-SPS-A24. Secondary phases are highlighted by red circles and white arrows.

observed in the microstructure of the annealed SPS samples (BTN-SPS-A12 and BTN-SPS-A24). The SEM-EDS data showed that both minor secondary phases contain Ba, Nb, and Ti, the same as the matrix phase (Fig. S-4 in the supplementary material). However, they have different ratios of Ba:Nb:Ti. The bright phase has a higher content of Ba compared to the matrix, and the dark phase shows more Ti and less Ba compared to the matrix. These changes in the (Ba, Nb, and Ti) levels explain their different contrast in the SEM images. As a result of the very short sintering time, the SPS-prepared samples exhibit small grain sizes, around $4.2\,\mu m$ for BTN-SPS-S, $5.8\,\mu m$ for BTN-SPS-A12, and $7.3\,\mu m$ BTN-SPS-A24. These values are much smaller than the average grain size of the ceramics prepared using conventional sintering.

2. Thermoelectric properties

The electrical conductivity of the Ar annealed SPS samples as a function of temperature is presented in Fig. 11(a). Both BTN-SPS-A12 and BTN-SPS-A24 show semiconductor conduction behavior from 350 K to ~723 K. At higher temperatures, the materials begin to show slight metallic behavior and a small reduction in conductivity with increasing temperature. BTN-SPS-A24 exhibits higher σ; the highest σ is ~40 S/cm at 873 K. The Seebeck coefficients for annealed SPS samples are presented in Fig. 11(b). The negative S values confirm the n-type nature of samples. With increasing temperature, all of the samples show an increase in the $|S|$ values. Within the uncertainty range, the S values for reduced SPS samples are not significantly affected by sintering or annealing conditions. At 873 K, the S value for annealed SPS samples reaches $-273\,\mu V/K$, which is much higher than values reported for other SPS-prepared tungsten bronze structured compounds.[24,25]

Compared to the pressureless sintered BTN samples, the SPS samples exhibit lower σ and higher $|S|$. To further understand the electrical conduction processes in BTN, the carrier concentration (n) was determined from S values with the aid of the modified Hiekes' equation[26] given by Eq. (3). The modified Hiekes' equation is based on the assumption that only one electron is permitted on a given site and both degeneracies of spin and orbital are negligible.[27] The contribution of vibrational entropy is assumed to be negligible. Therefore, the calculated values of carrier concentration are expected to be higher than the real values. The charge carrier mobility (μ) values were determined from the σ data using the relationship between σ, n, and μ given by Eq. (4),

$$n = c\left[\frac{1}{e^{S \cdot \frac{e}{k}} + 1}\right], \tag{3}$$

$$\mu = \sigma/(e \cdot n), \tag{4}$$

where c is the number of available sites for carriers per unit volume of the unit cell. For the tungsten bronze structured $Ba_6Ti_2Nb_8O_{30}$, c is equal to $8/V$, where V is the unit volume of the unit cell and can be calculated from the cell constant of the structure. The factor e/k is the ratio of the electronic charge to the Boltzmann constant and is approximately $1/86.2\,K/\mu V$; S is the Seebeck coefficients as shown in Fig. 11(b).

The calculated carrier concentrations and charge mobility data for both the conventional and SPS-prepared BTN samples are shown in Table II. The conventional BTN-A12 ceramic shows a high carrier concentration of $1.45 \times 10^{21}\,cm^{-3}$ and a high carrier
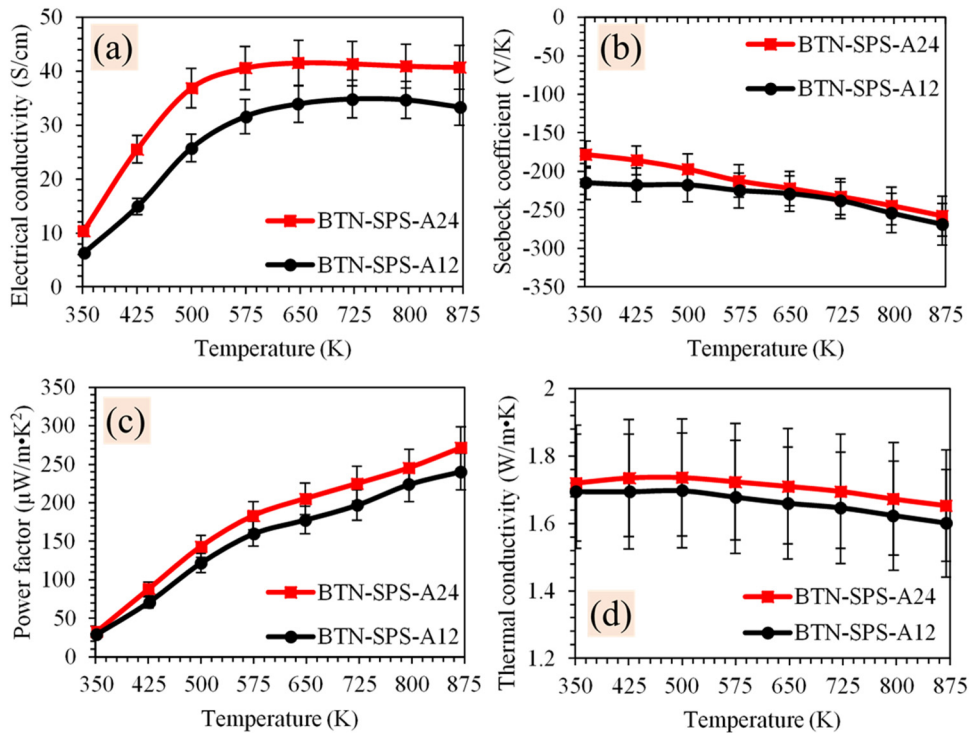
FIG. 11. Temperature dependence of thermoelectric properties of SPS-prepared $Ba_6Ti_2Nb_6O_{30}$ samples annealed in the reducing atmosphere. (a) Electrical conductivity, (b) Seebeck coefficient, (c) power factor, and (d) thermal conductivity.

mobility of $0.394 \, \text{cm}^2 \, \text{V}^{-1} \, \text{s}^{-1}$. The SPS-prepared samples had lower carrier concentrations, less than half that for the conventionally prepared samples. A possible reason is the lower annealing temperature used for the SPS-prepared samples. In terms of the carrier mobility, all of samples showed similar values. Therefore, the higher carrier concentrations in conventionally processed BTN ceramics is the primary reason for their higher σ and lower $|S|$ compared to the SPS samples.

The σS^2 values for SPS-prepared BTN samples are presented as a function of temperature in Fig. 11(c); all of the σS^2 values increase with temperature. For the SPS-prepared samples, the maximum σS^2 value of ${\sim}266 \, \mu\text{W/m K}^2$ at 873 K was achieved for BTN-SPS-A24. This is marginally lower than the value obtained for the conventionally sintered BTN-A12 ($286 \, \mu\text{W/m K}^2$). These results show that higher $|S|$ can be achieved for SPS samples in comparison to the conventional mixed oxide route. However, the reduced mechanical strength of the SPS samples (due to the secondary phase formation) limited the maximum annealing

temperature and, therefore, restricted the improvement in carrier concentration by the reduction process. It is still a challenge to compensate for the low electrical conductivity values due to the low carrier concentrations of the SPS samples.

The thermal conductivity of SPS-prepared BTN ceramics is presented in Fig. 11(d). Both of the BTN-SPS-A12 and BTN-SPS-A24 samples show low κ, with values of 1.8 and 1.7 W/m K, respectively, at 350 K; these reduce slightly at higher temperatures. Compared to the conventionally processed BTN ceramics, the SPS-prepared BTN ceramics exhibit a much lower κ. This is related to the smaller grain size and higher density of grain boundaries of the latter; the grain boundaries can act as phonon scattering sites.

The dimensionless figure of merit for reduced conventional and SPS-prepared samples of $Ba_6Ti_2Nb_8O_{30}$ ceramic is presented in Fig. 12. All samples show an increase in ZT with temperature. BTN-A12 and BTN-SPS-A24 show the maximum ZT (ZT_{max}) of ${\sim}0.14$ at 873 K. With the same annealing time, BTN-SPS-A12 exhibits slightly lower ZT values than BTN-A12, but the longer annealing time allows BTN-SPS-A24 to achieve similar ZT values to BTN-A12. In effect, the power factors and thermal conductivity data for the conventional and SPS-prepared samples (Figs. 8 and 10) are very similar. The main differences are that electrical conductivities are higher for conventionally prepared samples (Fig. 9) and Seebeck coefficients are higher for the SPS-prepared samples (Fig. 11). The compensation between the electrical conductivity and Seebeck coefficients means that the overall ZT performance (Fig. 12) is quite similar. These ZT values are competitive with many other tungsten bronze structured oxides, but, in general,

TABLE II. Carrier concentrations and mobility values for the BTN samples.

Sample	Carrier concentration (cm^{-3}) ($\pm10\%$)	Carrier mobility $(\text{cm}^2 \, \text{V}^{-1} \, \text{s}^{-1})$ ($\pm10\%$)
BTN-A6	9.13×10^{20}	0.299
BTN-A12	1.45×10^{21}	0.394
BTN-SPS-A12	5.41×10^{20}	0.385
BTN-SPS-A24	6.08×10^{20}	0.418

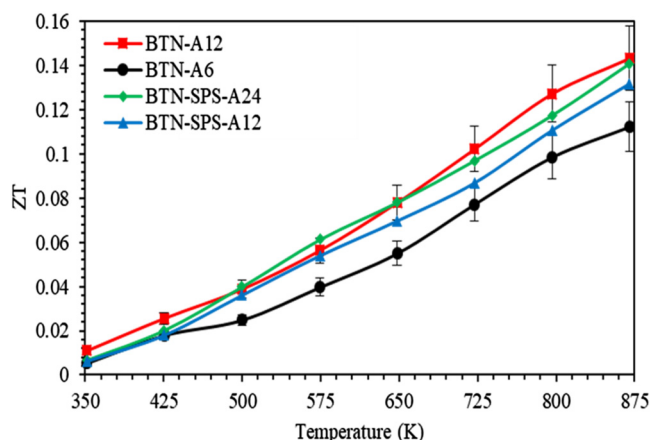**FIG. 12.** Dimensionless of figure of merit, ZT, values as a function of temperature for annealed $Ba_6Ti_2Nb_8O_{30}$ ceramics prepared via pressureless sintering and SPS.

the $Ba_6Ti_2Nb_8O_{30}$ ceramics have the advantage of a simpler preparation route.

IV. CONCLUSIONS

High quality $Ba_6Ti_2Nb_8O_{30}$ ceramics were prepared with 0.5 wt. % of MnO as a sintering aid by pressureless sintering and SPS. The crystal structure was resolved by employing a combination of synchrotron radiation and atomic resolution electron microscopy. BTN crystallizes with tetragonal symmetry with $a = 12.5407$ and $c = 4.0007$ Å in the $P4bm$ space group. Both pentagonal and tetragonal sites are fully occupied by Ba. Nb and Ti share positions in oxygen polyhedra with the Ti concentration being higher in 2b sites compared to 8d sites. A minor secondary phase $Ba(Ti_{0.46}Nb_{0.54})O_3$ was found in the 12-h Ar annealed BTN ceramics, which contributed to a decrease in the Ti occupancy on both B_1- and B_2-sites. The reduction in oxygen occupancy was only found at O(1), O(4), and O(5) positions.

The BTN ceramics showed phonon-glass-type conductivity behavior with modest electrical conductivity and low κ values of 1.7–1.65 W/m K from 350 to 873 K. A maximum ZT of 0.14 at 873 K was achieved for ceramics prepared by pressureless sintering and SPS. The thermoelectric properties of the tungsten bronze structured materials based on $Ba_6Ti_2Nb_8O_{30}$, especially the low thermal conductivities, are very encouraging. To progress them to be real candidates for thermoelectric applications now requires a significant enhancement of charge transport. The BTN ceramics offer the advantage of significantly easier processing than many of the TB structured materials.

SUPPLEMENTARY MATERIAL

Additional SEM images, EDS maps, HAADF STEM images, and crystal structure refinement data are included as supplementary material.

REFERENCES

[1] T. M. Tritt and M. A. Subramanian, MRS Bull. **31**, 188 (2006).
[2] W. M. Yim and A. Amith, Solid. State Electron. **15**, 1141 (1972).
[3] Y. Pei, A. LaLonde, S. Iwanaga, and G. J. Snyder, Energy Environ. Sci. **4**, 2085 (2011).
[4] Y. Gelbstein, Z. Dashevsky, and M. P. Dariel, Phys. B Condens. Matter **363**, 196 (2005).
[5] S. Lee, R. H. T. Wilke, S. Trolier-Mckinstry, S. Zhang, and C. A. Randall, Appl. Phys. Lett. **96**, 31910 (2010).
[6] S. Lee, S. Dursun, C. Duran, and C. A. Randall, J. Mater. Res. **26**, 26 (2011).
[7] Y. Li, J. Liu, Z. Wang, Y. C. Zhou, C. Wang, J. Li, Y. Zhu, M. Li, and L. Mei, Phys. Scr. **90**, 25801 (2015).
[8] Y. Li, J. Liu, Y. Zhang, Y. Chen, J. Li, W. Su, H. Wang, and C. Wang, Ceram. Int. **43**, 13345 (2017).
[9] Y. Li, Y. Zhang, J. Liu, Y. Chen, J. Li, W. Su, and C. Wang, J. Mater. Sci. Mater. Electron. **29**, 9137 (2018).
[10] F. Azough, R. Freer, S. R. Yeandel, J. D. Baran, M. Molinari, S. C. Parker, E. Guilmeau, D. Kepaptsoglou, Q. Ramasse, A. Knox, D. Gregory, D. Paul, M. Paul, A. Montecucco, J. Siviter, P. Mullen, W. Li, G. Han, E. A. Man, H. Baig, T. Mallick, N. Sellami, G. Min, and T. Sweet, J. Electron. Mater. **45**, 1894 (2015).
[11] N. C. Stephenson, Acta Crystallogr. **18**, 496 (1965).
[12] Y. Itoh and H. Iwasaki, J. Phys. Chem. Solid **34**, 1639 (1973).
[13] G. L. Roberts, R. J. Cava, W. F. Peck, and J. J. Krajewski, J. Mater. Res. **12**, 526 (1997).
[14] A. A. Coelho, J. Appl. Crystallogr. **33**, 899 (2000).
[15] S. A. Prosandeev, I. P. Paevski, and M. A. Bunin, Phys. Rev. B **70**, 157101 (2004).
[16] V. K. Trunov, I. M. Averina, and Y. A. Velikodnyi, Zh. Neorg. Khim. **25**, 1139 (1980).
[17] E. O. Chi, A. Gandini, K. M. Ok, L. Zhang, and P. S. Halasyamani, Chem. Mater. **16**, 3616 (2004).
[18] P. B. Jamieson and S. C. Abrahams, Acta Crystallogr. Sect. B **24**, 984 (1968).
[19] C. S. Dandeneau, Y. Yang, B. W. Krueger, M. A. Olmstead, R. K. Bordia, and F. S. Ohuchi, Appl. Phys. Lett. **104**, 101607 (2014).
[20] V. I. Nefedov, Y. V. Salyn, A. A. Chertkov, and L. N. Padurets, Zh. Neorg. Khim. **19**, 1443 (1974).
[21] B. Hessen, S. A. Sunshine, T. Siegrist, A. T. Fiory, and J. V. Waszczak, Chem. Mater. **3**, 528 (1991).
[22] G. Li, J. Yang, Y. Luo, Y. Xiao, L. Fu, M. Liu, and J. Peng, J. Am. Ceram. Soc. **96**, 2703 (2013).
[23] W. Tian and R. Yang, Comput. Model. Eng. Sci. **24**, 123 (2008).
[24] G. Cerretti, M. Schrade, X. Song, B. Balke, H. Lu, T. Weidner, I. Lieberwirth, M. Panthöfer, T. Norby, and W. Tremel, J. Mater. Chem. A **5**, 9768 (2017).
[25] R. Ottini, C. Tealdi, C. Tomasi, I. G. Tredici, A. Soffientini, U. Anselmi-Tamburini, P. Ghigna, and G. Spinolo, J. Appl. Phys. **121**, 85104 (2017).
[26] H. Taguchi, M. Sonoda, and M. Nagao, J. Solid State Chem. **137**, 82 (1998).
[27] H. L. Tuller and A. S. Nowick, J. Phys. Chem. Solids **38**, 859 (1977).